Dysregulated YAP1/TAZ and TGF-β signaling mediate hepatocarcinogenesis in *Mob1a/1b*-deficient mice

Miki Nishio[a], Keishi Sugimachi[b], Hiroki Goto[a], Jia Wang[a], Takumi Morikawa[a], Yosuke Miyachi[a], Yusuke Takano[a], Hiroki Hikasa[a], Tohru Itoh[c], Satoshi O. Suzuki[d], Hiroki Kurihara[e], Shinichi Aishima[f], Andrew Leask[g], Takehiko Sasaki[h], Toru Nakano[i], Hiroshi Nishina[j], Yuji Nishikawa[k], Yoshitaka Sekido[l], Kazuwa Nakao[m], Kazuo Shin-ya[n], Koshi Mimori[b,1], and Akira Suzuki[a,1,2]

[a]Medical Institute of Bioregulation, Graduate School of Medical Sciences, Kyushu University, Fukuoka, Fukuoka 819-0395, Japan; [b]Kyushu University Beppu Hospital, Beppu, Oita 874-0838, Japan; [c]Institute of Molecular and Cellular Biosciences, The University of Tokyo, Bunkyo, Tokyo 113-8654, Japan; [d]Graduate School of Medical Sciences, Kyushu University, Fukuoka, Fukuoka 819-0395, Japan; [e]Research Center for Advanced Science and Technology, The University of Tokyo, Bunkyo, Tokyo 113-8654, Japan; [f]Faculty of Medicine, Saga University, Saga, Saga 840-8502, Japan; [g]Schulich School of Medicine and Dentistry, University of Western Ontario, London, ON, Canada N6A 3K7; [h]Akita University Graduate School of Medicine, Akita, Akita 010-8502, Japan; [i]Medical School and Graduate School of Frontier Biosciences, Osaka University, Suita, Osaka 565-0871, Japan; [j]Medical Research Institute, Tokyo Medical and Dental University, Bunkyo, Tokyo 113-0034, Japan; [k]Asahikawa Medical University, Asahikawa, Hokkaido 078-8510, Japan; [l]Aichi Cancer Center Research Institute, Nagoya, Aichi 464-8681, Japan; [m]Medical Innovation Center, Graduate School of Medicine, Kyoto University, Kyoto, Kyoto 606-8501, Japan; and [n]National Institute of Advanced Industrial Science and Technology, Chiyoda, Tokyo 100-8921, Japan

Edited by Tak W. Mak, The Campbell Family Institute for Breast Cancer Research at Princess Margaret Cancer Centre, University Health Network, Toronto, Canada, and approved November 23, 2015 (received for review August 29, 2015)

Mps One Binder Kinase Activator (MOB)1A/1B are core components of the Hippo pathway that coactivate large tumor suppressor homolog (LATS) kinases. *Mob1a/1b* double deficiency in mouse liver (*L*Mob1DKO) results in hyperplasia of oval cells and immature cholangiocytes accompanied by inflammatory cell infiltration and fibrosis. More than half of mutant mice die within 3 wk of birth. All survivors eventually develop liver cancers, particularly combined hepatocellular and cholangiocarcinomas (cHC-CCs) and intrahepatic cholangiocellular carcinomas (ICCs), and die by age 60 wk. Because this phenotype is the most severe among mutant mice lacking a Hippo signaling component, MOB1A/1B constitute the critical hub of Hippo signaling in mammalian liver. *L*Mob1DKO liver cells show hyperproliferation, increased cell saturation density, hepatocyte dedifferentiation, enhanced epithelial–mesenchymal transition and cell migration, and elevated transforming growth factor beta(TGF-β)2/3 production. These changes are strongly dependent on Yes-Associated Protein-1 (*Yap1*) and partially dependent on PDZ-binding motif (*Taz*) and *Tgfbr2*, but independent of connective tissue growth factor (*Ctgf*). In human liver cancers, YAP1 activation is frequent in cHC-CCs and ICCs and correlates with SMAD family member 2 activation. Drug screening revealed that antiparasitic macrocyclic lactones inhibit YAP1 activation in vitro and in vivo. Targeting YAP1/TAZ with these drugs in combination with inhibition of the TGF-β pathway may be effective treatment for cHC-CCs and ICCs.

MOB1 | Hippo pathway | liver cancer | ivermectin | TGF-beta

Liver cancer is the third leading cause of cancer death in humans (1, 2). Hepatocellular carcinoma (HCC) and intrahepatic cholangiocellular carcinoma (ICC) are the first and second most common liver cancers in humans, whereas combined hepatocellular and cholangiocarcinomas (cHC-CCs) occur at rare frequency (3). For unknown reasons, patients with ICC and cHC-CC have much worse prognoses than HCC patients (3). Although molecularly targeted agents increase the survival of patients with advanced HCC, ICC and cHC-CC patients rarely show clinical responses to these drugs. Therefore, elucidation of the molecular mechanisms driving the onset/progression of ICCs and cHC-CCs and the identification of targeted agents effective against these tumors are eagerly awaited.

The Hippo signaling pathway was first identified as regulating organ size in *Drosophila* (4). In mammals, most components of the Hippo pathway have been implicated as tumor suppressors, including neurofibromin-2 (NF2), the mammalian STE20-like protein (MST) kinases, the large tumor suppressor homolog (LATS) kinases, and the adaptor proteins Salvador Homolog-1 (SAV1) and Mps One Binder Kinase Activator (MOB). MOB is considered to be one of four core Hippo pathway components. Structurally, MOB is an adaptor protein with no apparent functional domain. However, phosphorylation of MOB by MST allows MOB to bind to LATS, and this binding greatly increases the phosphorylation and kinase activity of LATS (5). Downstream of MOB and LATS are two paralogous transcriptional coactivators: Yes-Associated Protein-1 (YAP1) and transcriptional coactivator with PDZ-binding motif (TAZ), which drive the expression of numerous effector genes (6).

Activation of the Hippo pathway occurs in response to increased cell density and decreased extracellular matrix rigidity or mechanical forces (7). In the presence of MOB1, LATS1/2 strongly phosphorylates YAP1/TAZ, which binds to 14-3-3 protein. This binding draws phosphorylated YAP1/TAZ into the cytoplasm (8),

Significance

Patients with intrahepatic cholangiocellular carcinoma (ICC) and combined hepatocellular and cholangiocarcinoma (cHC-CC) have worse prognoses than those with hepatocellular carcinoma and rarely show clinical responses to drugs. Our analyses of mice with liver-specific deletions of Mps One Binder Kinase Activator (MOB)1A/1B reveal that MOB1A/1B constitute the most important hub of Hippo signaling in mammalian liver. MOB1A/1B maintain hepatocyte stem/progenitor cell quiescence and are potent tumor suppressors, especially in cHC-CCs and ICCs. Because these functions depend on the Hippo target *Yap1/Taz* and the *Yap1/Taz* targets *Tgfbs*, our data point to a new therapeutic approach for liver cancer based on inhibition of MOB1-YAP1/TAZ and/or TGF-βs–SMADs signaling. Our demonstration that well-tolerated and already-approved antiparasitic drugs inhibit YAP1 signaling may point to a new route of treatment for these cancers that can be rapidly tested and implemented.

Author contributions: M.N., K.M., and A.S. designed research; M.N., K.S., H.G., J.W., T.M., Y.M., Y.T., H.H., and K.S.-y. performed research; T.I., H.K., A.L., T.S., Y.N., and Y.S. contributed new reagents/analytic tools; M.N., K.S., T.I., S.O.S., S.A., T.N., H.N., Y.N., K.N., K.S.-y., K.M., and A.S. analyzed data; and A.S. wrote the paper.

The authors declare no conflict of interest.

This article is a PNAS Direct Submission.

Freely available online through the PNAS open access option.

[1]K.M. and A.S. contributed equally to this work.

[2]To whom correspondence should be addressed. Email: suzuki@bioreg.kyushu-u.ac.jp.

This article contains supporting information online at www.pnas.org/lookup/suppl/doi:10.1073/pnas.1517188113/-/DCSupplemental.

preventing it from activating TEA domain family member (TEAD)-mediated transcription of connective tissue growth factor (*CTGF*) (9), secreted phosphoprotein 1 (*SPP1*) (10), transforming growth factor beta (*TGFβ*) (11), and Jagged 1 (*JAG1*) (12). Phosphorylated YAP1/TAZ also binds to E3-ubiquitin ligase $SCF^{\beta TRCP}$ and is degraded (13). Thus, YAP1/TAZ are positive regulators of cell proliferation that are suppressed by Hippo signaling.

Hippo signaling is important for stem cell quiescence. Mice with liver-specific deletion of *Nf2* (14), *Sav1* (15, 16), or *Mst1/2* (17, 18), or mice with transgenic *Yap1* expression (19–21), show not only liver tumors but also hepatocyte dedifferentiation (22), increased liver stem/progenitor cells, and hepatomegaly. However, the precise roles of mammalian Hippo signaling components have been difficult to identify, partly because multiple homologs of each element exist. It is not clear why deficiency for almost any one homolog is embryonic-lethal in mice despite the presence of multiple homologs of each element. In addition, the function of a given Hippo component may differ in different tissues or even in different studies. For example, Benhamouche et al. (14) reported that the liver phenotype of $Nf2^{-/-}$ mice depends on NF2-EGFR signaling rather than on the NF2-MOB1-LATS-YAP1 pathway, but another study found that the $Nf2^{-/-}$ liver phenotype could be rescued by heterozygous deletion of *Yap1* (23). Similarly, the skin phenotype associated with abnormal Hippo signaling depends on SAV1 (16) and YAP1, but is independent of MST1/2 (24). Therefore, the in vivo function of each mammalian Hippo pathway component in each tissue must be clarified separately.

In this study, we focused on liver-specific loss of *Mob1a/1b*. Among seven MOB homologs in humans, only hMOB1A and hMOB1B bind to LATS1/2 and promote their activation (25). MOB1A and MOB1B share 95% amino acid identity, are substrates of the ubiquitin ligase PRAJA2 (26), and are commonly decreased in tumors. *hMOB1A* is mutated in melanoma and breast cancer cell lines and down-regulated in human colorectal, nonsmall cell lung, and skin cancers (27, 28). Surprisingly, impaired MOB1 phosphorylation occurs in 81% of human liver cancers (17), and elevated YAP1 is now an independent prognostic marker for these malignancies (29). In mice, MOB1B can compensate for loss of MOB1A, and vice versa, but loss of both *Mob1a* and *Mob1b* is embryonic-lethal (28). Mice partially deficient for *Mob1a/1b* develop tumors, most often skin cancers (28). However, the physiological functions of MOB1A/1B in liver are unknown, and the liver abnormalities of NF2-, SAV1-, or MST1/2-deficient mice had been thought to be independent of MOB1A/1B and LATS1/2 (17).

TGF-βs regulate cell growth, apoptosis, differentiation, and fibrosis (30). TGF-βs inhibit the proliferation of normal epithelial cells but display both tumor-suppressing and tumor-promoting activities during cancer development (31). The binding of TGF-β1–3 to TGF-β receptor-2 (TGFBR2) activates TGFBR1, which activates the SMADs pathway transmitting the signal into the nucleus (32). Nuclear SMAD2/3 activity is enhanced by nuclear translocation of YAP1/TAZ, whereas cytoplasmic YAP1/TAZ prevents the nuclear accumulation of SMADs (33, 34).

Here, we analyze the role of MOB1A/1B in mouse liver and show that disruption of MOB1 drives hyperplasia of oval cells and immature cholangiocytes, as well as the development of cHC-CC and ICC in a manner inhibited by the targeting of YAP1/TAZ and TGF-β–SMADs. Importantly, we identify two well-tolerated, antiparasitic macrocyclic lactones as effective YAP1 inhibitors in vitro and in vivo.

Results

Loss of *Mob1a/1b* in Murine Liver Results in Hyperplasia of Oval Cells/Immature Cholangiocytes and Early Lethality. We generated liver-specific *Mob1a/1b*-deficient mice (*L*Mob1DKO mice) by crossing $Mob1a^{flox/flox};Mob1b^{-/-}$ mice to *AlbCre*-Tg mice (35). Southern blotting confirmed disruption of the $Mob1a^{flox}$ allele in most liver cells of *L*Mob1DKO mice, leaving the $Mob1a^{\Delta}$ allele (Fig. S1*A*). Crossing of *L*Mob1DKO mice with *Rosa26-LSL-YFP* reporter mice (36) confirmed that most cholangiocytes and hepatocytes had undergone *Mob1a/1b* deletion, as determined by YFP-positivity and PCR analysis following laser microdissection (Fig. S1 *B* and *C*).

From postnatal day (P) 10 (P10) onward, *L*Mob1DKO mice displayed abdominal swelling due to massive hepatomegaly (Fig. 1 *A* and *B*). The total number of liver cells in *L*Mob1DKO mice was five times that in controls at P14 (Fig. 1*C*). The first *L*Mob1DKO mice died at P14, and more than half were dead by P21 (Fig. 1*D*).

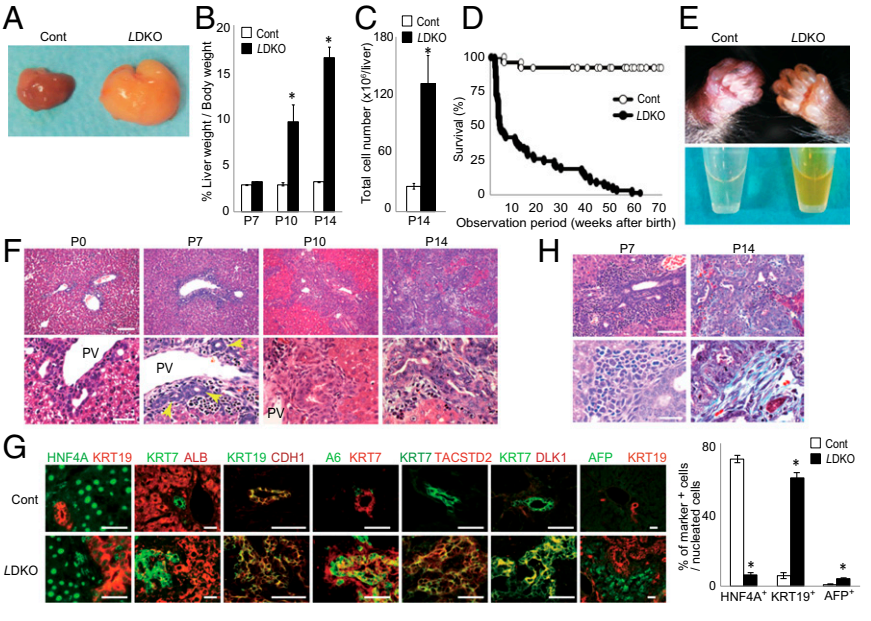

Fig. 1. Hyperplasia of immature cholangiocytes in the absence of *Mob1a/1b*. (*A*) Macroscopic analyses of livers from $Mob1a^{flox/flox};Mob1b^{-/-}$ (control, Cont) and $AlbCre;Mob1a^{flox/flox};Mob1b^{-/-}$ (*L*Mob1DKO; *L*DKO) mice at P10 ($n = 7$). (*B*) Liver weight as a percentage of body weight for the mice in *A* at the indicated ages. Data are the mean ± SEM ($n = 7$). *$P < 0.01$. (*C*) Absolute total liver cell numbers for the mice in *B* at P14. Data are the mean ± SEM ($n = 6$). *$P < 0.01$. (*D*) Kaplan–Meier survival analysis of control ($n = 26$) and *L*DKO ($n = 69$) mice. (*E*) Representative images of (*Upper*) jaundice in the skin and (*Lower*) yellow-colored serum from the P14 *L*DKO mice. (*F*) Histology of *L*DKO liver sections at the indicated ages. Lower panels (scale bar, 50 μm) are higher-magnification images of the upper panels (scale bar, 100 μm). Yellow arrows, immature cholangiocytes with luminal structure. PV, portal vein. Results are representative of 20 livers per group. (*G*) (*Left*) Immunohistochemical analysis of the indicated markers in a control and *L*DKO liver at P10. Results are representative of five livers per group. (Scale bars, 50 μm.) (*Right*) Percentages of $KRT19^+$, $HNF4A^+$, and AFP^+ cells in livers of the control and *L*DKO mice in the left panel. Data are the mean ± SEM ($n = 5$). *$P < 0.01$. (*H*) (*Left*) H&E-stained P7 *L*DKO liver. (*Right*) H&E-stained P14 *L*DKO liver counterstained with Masson trichrome. Lower panels (scale bar, 20 μm) are higher-magnification images of the upper panels (scale bar, 50 μm). Results are representative of 10 livers per group. For all panels of all figures, results are representative of ≥3 independent trials involving three or more mice per group.

The skin of the mutant mice was jaundiced, and their serum was yellow in color due to elevated bilirubin (Fig. 1*E* and Fig. S1*D*), suggesting that defective liver function was likely the cause of death. Histological examination revealed no obvious structural abnormalities in livers of *L*Mob1DKO mice at P0. However, immature cholangiocyte-like cells increased in mutant liver from P7, and massive accumulations of these cells were observed from P10, especially in periductal and intraductal locations (Fig. 1*F*). Although some mutant cholangiocyte-like cells started to form luminal structures, most were too immature to do so. The penetrance of these phenotypes was complete in *L*Mob1DKO mice, and immature cholangiocyte-like cells were never observed in control mice ($Mob1a^{flox/flox}$;$Mob1b^{-/-}$), *AlbCre*-Tg mice, or in single KO mice with systemic deletion of *Mob1a* ($Mob1a^{\Delta/\Delta}$) or *Mob1b* ($Mob1b^{-/-}$) (Fig. S2 *A* and *B*). Immunostaining revealed that the cholangiocyte-like cells abundant in *L*Mob1DKO liver expressed the cholangiocyte lineage markers KRT19, KRT7 and CDH1, and that some also bore the oval cell markers A6, TACSTD2, and DLK (Fig. 1*G*). Oval cells, which are stem/progenitor cells of hepatocytes and cholangiocytes (37), are not observed in healthy adult liver but appear in response to liver injury (38). Immature AFP^+ hepatocytes were also present in *L*Mob1DKO liver, as were infiltrating inflammatory cells and fibrosis (Fig. 1*H*). However, because the oval cell/cholangiocyte accumulations occurred in portal and intraductal locations where oval cells usually reside (39), and did not form a tumor mass at P14, *L*Mob1DKO livers were deemed to exhibit "oval cell and immature cholangiocyte hyperplasia."

Surviving *L*Mob1a/1a KO Mice Succumb to cHC-CCs and ICCs. Most *L*Mob1DKO mice surviving beyond P21 exhibited mild hepatocholangiocellular hyperplasia. Although these animals had a long lifespan, they all eventually developed hepatocellular adenomas, HCCs, ICCs or cHCC-CCs (Fig. 2). About 80% (8/10) of surviving *L*Mob1DKO mice showed these tumors by age 15 wk, and all such mutants were dead by 60 wk due to multifocal cHC-CCs (59%; 13/22), ICCs only (23%; 5/22), or HCCs only (18%; 4/22). Tumors containing transitional cells intermediate between HCC and ICC (Fig. 2*C*), and occurrences of HCC and ICC within the same liver (Fig. 2*B*), resembled cases of human cHC-CC and so were classified as cHC-CCs. About 15% (2/13) of tumor-bearing mutants >40 wk of age showed lung metastasis (Fig. 2*C*). Equivalent but milder histological changes, including the presence of cHC-CCs and ICCs, occurred in livers of inducible *AlbCreER;* $Mob1a^{flox/flox}$;$Mob1b^{-/-}$ mice (*Materials and Methods*) treated with tamoxifen (+Tmx) at 5 wk of age (Fig. S2 *C* and *D*).

Tumorigenic Properties of *Mob1a/1b*-Deficient Liver Cells. To determine whether *Mob1a*/*1b*-deficient liver cells showed increased proliferation, we administered BrdU to WT and *L*Mob1DKO mice at P10 and analyzed BrdU incorporation by liver cells 1 h later. An increase in $BrdU^+$ proliferating cells occurred among $KRT19^+$ oval cells/immature cholangiocytes (four times control levels) and $HNF4A^+$ (hepatocyte nuclear factor-4 alpha) hepatocytes (three times control levels) of *L*Mob1DKO mice (Fig. 3*A*), but $TUNEL^+$ apoptotic cells were very rare both in control and *L*Mob1DKO liver (Fig. S3*A*).

We next examined a Tmx-inducible murine *Mob1a*/*1b* DKO bipotential liver progenitor cell clone (*im*Mob1DKOLP) that arose by spontaneous immortalization of liver cells from *Rosa26CreER;* $Mob1a^{flox/flox}$;$Mob1b^{-/-}$ mice cultured without Tmx (−Tmx) (Fig. S3*B*). These cells are $HNF4A^+$, ALB^{dim}, $KRT19^+$, $KRT7^{dim}$, $CDH1^+$, $TACSTD2^{dim}$, DLK^{dim}, KIT^+, and $THY1^{dim}$, but $CD45^-$ and $CD31^-$ (Fig. S3*C*). *im*Mob1DKOLP cells undergo biliary cell differentiation when cultured in collagen-1 gel containing TNFα but become hepatocytes when cultured in matrigel containing Oncostatin M (Fig. S3 *D* and *E*). After Tmx administration (+Tmx; induces *Mob1a*/*1b* deletion), the proliferation and saturation density of *im*Mob1DKOLP cells increased (Fig. 3*B*) with no difference in cell size (Fig. S3*F*), suggesting that *im*Mob1DKOLP+Tmx cells have a defect in cell contact inhibition. Moreover, these cells formed numerous multilayered foci after prolonged culture (Fig. 3*C*) and rapidly generated tumors in vivo after xenografting into *nude* mice (Fig. S3*G*).

RT-PCR examination revealed that *im*Mob1DKOLP+Tmx cells showed increased mRNA levels of the stem cell markers *Tacstd2* and *Dlk1* and the cholangiocellular markers *Krt7*, *Krt19*, *Intb4*, and *Aqp1* but decreased mRNA levels of the mature hepatocyte markers *Hnf4α*, *Alb*, *Ttr*, and *Tat* (Fig. 3*D*). Because this

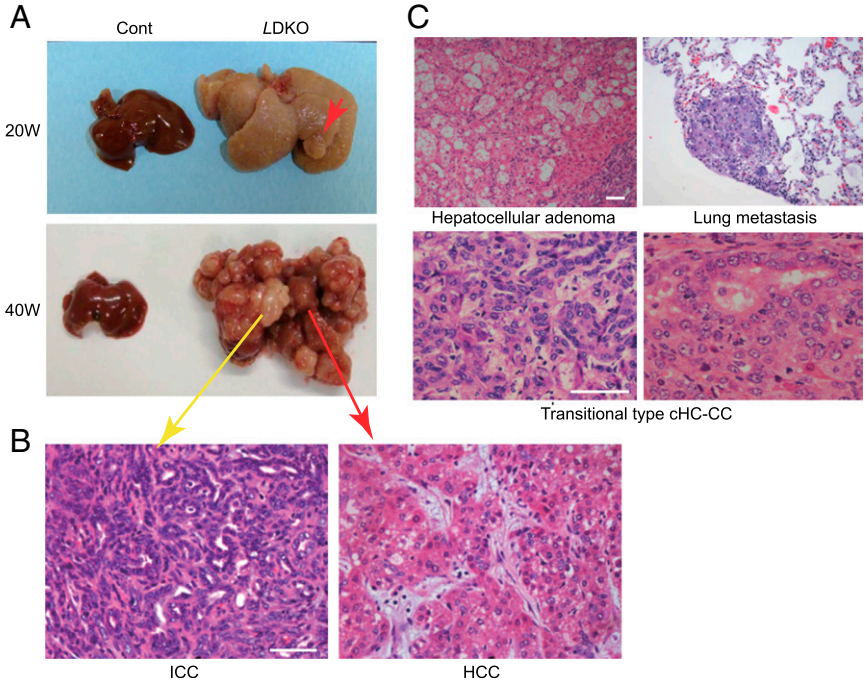

Fig. 2. Liver tumors observed in *L*Mob1DKO mice. (*A*) Macroscopic views of representative livers from 20- or 40-wk-old control and *L*DKO mice ($n = 7$). Red arrows, HCC; yellow arrow, ICC. (*B*) H&E-stained ICC and HCC from a 40-wk-old *L*DKO mouse in *A*. (Scale bar, 50 μm.) (*C*) H&E-stained tumor types in *L*DKO livers: hepatocellular adenoma (15-wk-old mouse); transitional type cHC-CC (40 wk); and lung metastasis (40 wk). (Scale bars, 50 μm.)

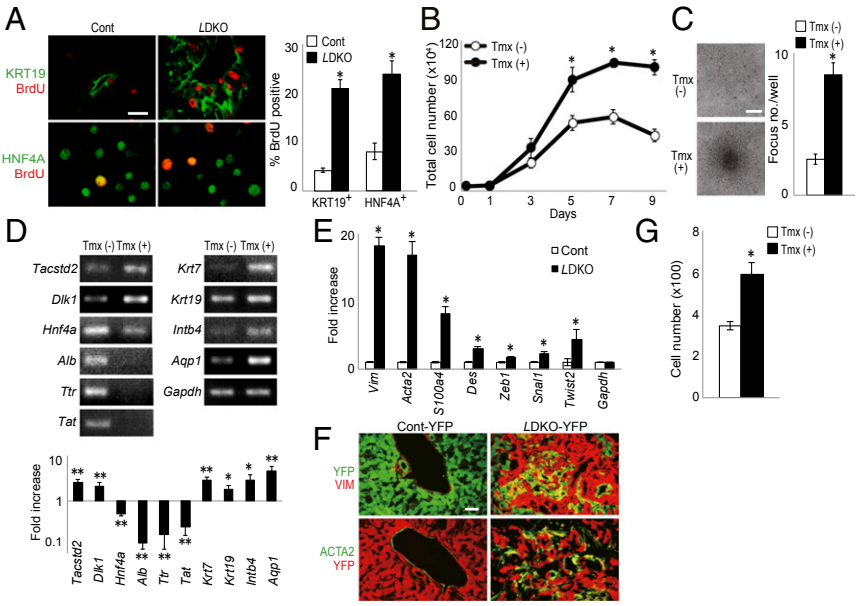

Fig. 3. Tumorigenic anomalies in liver cells of *L*Mob1DKO mice. (*A*) (*Left*) Immunostaining to detect BrdU incorporation (red) in P10 control and *L*DKO livers at 1 h post-BrdU injection. Cells were counterstained (green) with (*Top*) anti-KRT19 or (*Bottom*) anti-HNF4A Ab. (Scale bar, 20 μm.) (*Right*) Percentage of BrdU$^+$ cells among the KRT19$^+$ or HNF4A$^+$ cells in the left panel. Data are the mean ± SEM ($n = 5$). *$P < 0.01$. (*B*) Total numbers of *im*Mob1DKOLP cells cultured for the indicated number of days ± Tmx (1 μM). Data are the mean ± SEM of triplicate cultures. *$P < 0.01$. (*C*) (*Left*) Morphology of *im*Mob1DKOLP cells cultured for 7 d in the absence [Tmx (–)] or presence [Tmx (+)] of Tmx (1 μM). Multiple foci are visible in the *im*Mob1DKOLP+Tmx culture. (Scale bar, 200 μm.) (*Right*) Number of foci per well in the cultures in the left panel. Data are the mean ± SEM ($n = 11$). *$P < 0.01$. (*D*) RT-PCR (*Upper*) and mRNA levels (*Lower*) of the indicated markers in *im*Mob1DKOLP cells cultured ± Tmx for 10 d. *Tacstd2* and *Dlk1*, markers of liver stem/progenitor cells; *Hnf4a*, *Alb*, *Ttr*, and *Tat*, mature hepatocyte markers; *Krt7*, *Krt19*, *Intb4*, and *Aqp1*, cholangiocyte markers. *$P < 0.05$, **$P < 0.01$. (*E*) mRNA levels of the indicated EMT-related genes in P14 control and *L*DKO livers. Data are the mean ± SEM ($n = 4$). *$P < 0.01$. (*F*) Immunostaining to detect the indicated mesenchymal cell marker proteins in YFP$^+$ epithelial cells in liver sections from P14 *AlbCre;Mob1a$^{+/+}$;Mob1b$^{-/-}$;Rosa26-LSL-YFP* (Cont-YFP) mice and *AlbCre;Mob1a$^{flox/flox}$;Mob1b$^{-/-}$;Rosa26-LSL-YFP* (*L*Mob1DKO-YFP) mice ($n = 4$). (*G*) Cell migration assay of *im*Mob1DKOLP cells ± Tmx (1μM) determined using a Transwell assay. The number of cells that had migrated into the bottom chamber after 24 h was counted in four fields under light microscopy. Data are the mean ± SEM ($n = 3$ chambers per group). *$P < 0.01$.

cloned cell line maintained a homogeneous cell shape and uniform staining, we speculated that the increase in immature cells in *L*Mob1DKO liver might be due to hepatocyte dedifferentiation into oval cells and immature cholangiocytes.

RT-PCR examination of P14 *L*Mob1DKO liver cells showed enhanced expression of mesenchymal cell markers (*Vim*, *Acta2*, *S100a4*, and *Des*) and transcriptional factors (*Zeb1*, *Snal1*, and *Twist2*) important for the epithelial–mesenchymal transition (EMT) (Fig. 3*E*). Immunostaining demonstrated that spindle-shaped YFP$^+$VIM$^+$ and YFP$^+$ACTA2$^+$ EMT cells were present in P14 livers of *AlbCre;Mob1a$^{flox/flox}$;Mob1b$^{-/-}$;Rosa26-LSL-YFP* (*L*Mob1DKO-YFP) mice but rare in control *AlbCre;Mob1a$^{+/+}$;Mob1b$^{-/-}$;Rosa26-LSL-YFP* (Control-YFP) livers (Fig. 3*F*). In addition, the migration of *im*Mob1DKOLP+Tmx cells in Transwell chambers was enhanced compared with *im*Mob1DKOLP-Tmx cells (Fig. 3*G*). Finally, although not statistically significant, expression levels of epithelial markers such as *Cdh1* and *Tjp1* tended to be decreased in *L*Mob1DKO liver compared with controls (Fig. S3*H*). This lack of significance may be due to the limited area of enhanced EMT present in *L*Mob1DKO liver. In any case, our data suggest that elevated cell proliferation, impaired contact inhibition, augmented dedifferentiation, enhanced EMT, and increased cell migration may underlie the higher numbers of oval cells/immature cholangiocytes and liver tumor development seen in *L*Mob1DKO mice.

Enhanced YAP1/TAZ and TGF-βs Activation in *Mob1a/1b*-Deficient Liver Cells. We next investigated the effects of *Mob1a/1b* loss on Hippo components using *im*Mob1DKOLP cells cultured at high density to achieve saturation. As expected, *im*Mob1DKOLP+Tmx cells showed reduced phosphorylation of YAP1 (Ser127) and TAZ (Ser89) and increased total YAP1 and TAZ proteins under these culture conditions (Fig. 4*A*). Quantitative RT-PCR analysis established that these changes were not due to altered YAP and TAZ mRNA levels (Fig. S4*A*). Phospho-LATS1 (T1079) was below the assay detection limit but total LATS1 was reduced in *im*Mob1DKOLP+Tmx cells (Fig. 4 *A* and *B*). No differences in phospho-MST1, total MST1, or total SAV1 were detected. We then stimulated *im*Mob1DKOLP ± Tmx cells with okadaic acid (OA), which activates MST1/2 (40), and performed immunoblotting after adjusting lysates to equality of LATS1 protein. Whereas OA-stimulated *im*Mob1DKOLP-Tmx cells showed vigorous LATS1 phosphorylation, OA-stimulated *im*Mob1DKOLP+Tmx cells did not (Fig. 4*B*).

*im*Mob1DKOLP-Tmx cells cultured at high cell density showed cytoplasmic localization and inactivation of YAP1, as expected (Fig. 4*C*). However, YAP1 remained activated and positioned in the nucleus in high-density *im*Mob1DKOLP+Tmx cells. Similarly, most oval cells/immature cholangiocytes and hepatocytes in *L*Mob1DKO livers showed nuclear YAP1, unlike controls (Fig. 4*D*). Thus, MOB1 promotes density-induced cytoplasmic localization of YAP1, and MOB1A/1B deficiency drives nuclear localization of YAP1.

We compared control and *L*Mob1DKO livers using microarray and found a greater than fivefold increase in several growth factors and chemokines. High mRNA levels of *Ctgf*, *Spp1*, *Jag1*, *Tgfb2/3*, and *Ccl2*, which are all downstream YAP1/TAZ transcriptional targets, occurred in MOB1A/1B-deficient liver (Fig. 4*E*). Immunoblotting confirmed up-regulation of these proteins (except CCL2) in *L*Mob1DKO liver, as well as elevation of phospho-SMAD2 (Fig. 4*F*). However, activated NOTCH1 (NOTCH1IC), NOTCH2IC, and their downstream target HES1, which are all important for the conversion of hepatocytes into primitive ductular cells (41), were not altered even though JAG1 (Notch ligand) was increased (Fig. 4*F*). Immunostaining of *Mob1a/1b*-deficient livers revealed that CTGF, JAG1, and SPP1 (Fig. 4*G*), as well as phospho-SMAD2 and nuclear SMAD2/3 (Fig. 4*H*), were all enhanced in oval cells/immature cholangiocytes. TGF-β2/3, phospho-SMAD2, and nuclear SMAD2/3 were increased in mutant hepatocytes, and TGF-β3 was also elevated in inflammatory cells. Thus, heightened activation of YAP1/TAZ, CTGF, TGF-βs–SMADs, JAG1, and SPP1 may contribute to the abnormalities in *L*Mob1DKO liver. Alternatively, the observed increase in growth factors such as CTGF, JAG1, and SPP1, especially in immature cholangiocytes, may be secondary to the increased number of oval cells in *L*Mob1DKO liver.

***Mob1a/1b*-Deficient Liver Phenotypes Depend on YAP1, TAZ, and TGF-βs.** To determine whether *Mob1a/1b*-deficient liver phenotypes depended on activation of YAP1/TAZ, TGF-βs–SMAD2/3, and/or CTGF, we generated triple knockout (TKO) mice: *Mob1a/1b* plus *Yap1* (*AlbCre;Mob1a$^{flox/flox}$;Mob1b$^{-/-}$;Yap1$^{flox/flox}$*); *Mob1a/1b* plus *Taz* (*AlbCre;Mob1a$^{flox/flox}$;Mob1b$^{-/-}$;Taz$^{-/-}$*); *Mob1a/1b* plus *Tgfbr2* (*AlbCre;Mob1a$^{flox/flox}$;Mob1b$^{-/-}$;Tgfbr2$^{flox/flox}$*); and *Mob1a/1b*

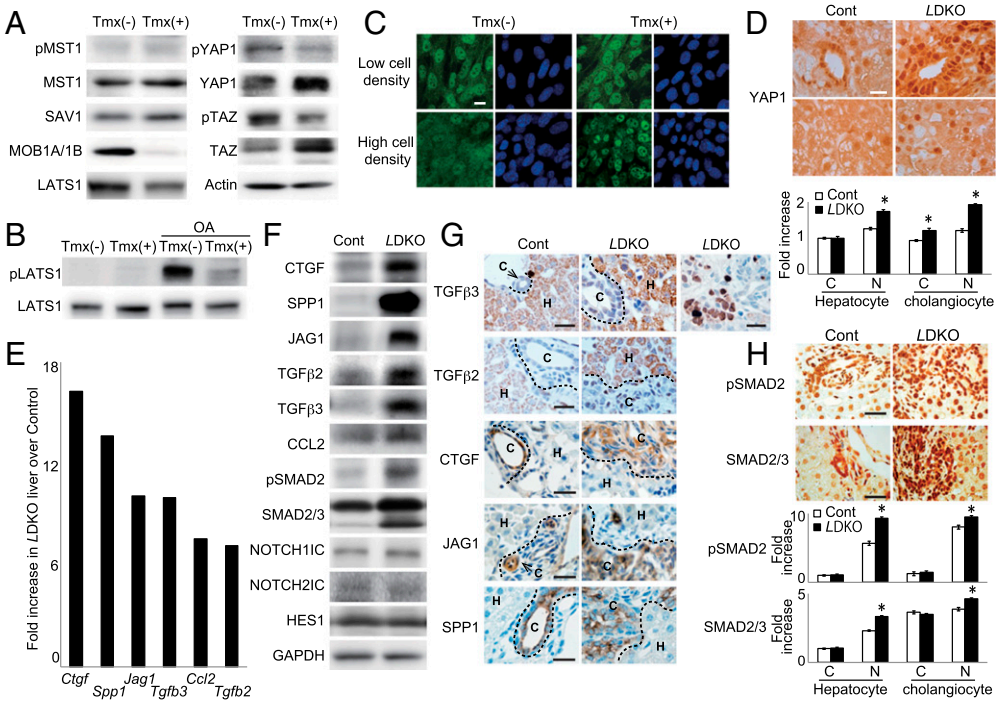

Fig. 4. Mob1-mediated regulation of YAP1/TAZ controls liver homeostasis. (*A*) Immunoblot detecting the indicated Hippo pathway proteins in *im*Mob1DKOLP ± Tmx cells at 5 d post-Tmx. Actin, loading control. (*B*) Immunoblot detecting pLATS1 protein in *im*Mob1DKOLP ± Tmx cells that were left untreated or treated with OA for 30 min. Total LATS1 protein levels in each sample were adjusted to equality before electrophoresis. (*C*) Immunostaining to detect YAP1 (green) in *im*Mob1DKOLP ± Tmx cells cultured at low or high cell density. DAPI (blue), nuclei. (Scale bar, 10 μm.) (*D*) (*Upper*) Immunostaining to detect YAP1 in the portal area (*Top*) and intrahepatic lobule area (*Bottom*) of P10 control and *L*DKO livers. (Scale bar, 20 μm.) (*Lower*) Densitometric determination of the intensities of cytoplasmic (C) and nuclear (N) YAP1 staining in the control and *L*DKO hepatocytes and cholangiocytes in the upper panel. Data are the mean ± SEM ($n = 15$). *$P < 0.01$. (*E*) mRNA levels of the indicated growth factor and chemokine genes in control vs. *L*DKO liver. Genes showing a greater than fivefold increase in *L*DKO liver over controls as determined by microarray are shown. (*F*) Immunoblot detecting the indicated proteins in the control and *L*DKO livers in *E*. GAPDH, loading control. (*G*) (*Left*) Immunostaining to detect the indicated proteins in P10 control and *L*DKO livers. H, hepatocyte. C, cholangiocyte. (Scale bars, 20 μm.) (*H*) (*Upper*) Immunostaining to detect pSMAD2 and total SMAD2/3 in P10 control and *L*DKO livers. (Scale bars, 20 μm.) (*Lower*) Densitometric determination of the intensities of cytoplasmic (C) and nuclear (N) pSMAD2 and SMAD2/3 staining in the control and *L*DKO hepatocytes and cholangiocytes in the upper panel. Data are the mean ± SEM ($n = 10$). *$P < 0.01$.

plus *Ctgf* (*AlbCre;Mob1a*$^{flox/flox}$;*Mob1b*$^{-/-}$;*Ctgf*$^{flox/flox}$). The increases in liver weight, numbers of oval cells/immature cholangiocytes, and liver fibrosis seen in *L*Mob1DKO mice were dramatically suppressed by additional *Yap1* loss (Fig. 5 *A* and *B*). However, at P14, these triple mutants still exhibited some oval cell/cholangiocellular hyperplasia and fibrosis, indicating that *Yap1* deletion cannot rescue the *L*Mob1DKO phenotype completely. All *L*Mob1a/1b;*Yap1* TKO mutants survived for at least 20 wk without developing liver cancers, whereas >80% of *L*Mob1DKO mice show tumors or lethality by this age (Fig. 1*D*). *L*Mob1a/1b; *Taz* TKO (Fig. 5*C*) and *L*Mob1a/1b;*Tgfbr2* TKO (Fig. 5*D*) mice displayed partial suppression of abnormalities associated with *Mob1a/1b* loss. However, *L*Mob1a/1b;*Ctgf* TKO (Fig. 5*E*) mice showed the same range of liver abnormalities as *L*Mob1DKO mice. Thus, the liver phenotypes of *L*Mob1DKO mice are strongly dependent on YAP1 and partly dependent on TAZ and TGF-βs, but not significantly dependent on CTGF.

Because YAP1 and TAZ are coactivators of TEAD1–4, we suspected that the proliferation occurring in the absence of MOB1A/1B was TEAD-mediated. siRNA analysis of *im*Mob1DKOLP+Tmx cells showed that their enhanced proliferation was suppressed by treatment with siYap1/Taz or siTead1/4 (Fig. S4 *B–E*). Addition of TGF-β2 did not alter the proliferation of *im*Mob1DKOLP+Tmx cells but did increase their expression of mesenchymal/cholangiocyte markers while decreasing hepatocyte markers, consistent with a previous report (42) and their enhanced YAP1 activation (Fig. S5 *A–D*). In *L*Mob1a/1b;*Tgfbr2* TKO mice, the additional loss of *Tgfbr2* decreased the YAP1 activation induced by *Mob1a/1b* deficiency in vivo (Fig. S5 *E* and *F*). Consistent with this observation, treatment in vitro of *im*Mob1DKOLP+Tmx cells with the TGF-βRI inhibitor SB431542 also decreased YAP1 activation (Fig. S5*G*).

Thus, considering that (*i*) TGF-βs production is increased by YAP1/TAZ activation (11), (*ii*) nuclear SMAD2/3 activity is enhanced by nuclear translocation of YAP1/TAZ (33), and (*iii*) YAP1 is activated by TGF-βs, we believe that the TGF-β pathway contributes to YAP1 activation via a positive feedback loop. The elevated TGF-β2 and TGF-β3 in *L*Mob1DKO liver may promote EMT and drive hepatocyte dedifferentiation toward immature cholangiocytes, and it is these cells that invade the liver parenchyma.

YAP1 and TGF-βs–SMADs in Human cHC-CCs and ICCs and Drugs Targeting Hippo Signaling. Abnormalities in Hippo components occur in many types of human tumors (43). We immunostained liver samples from patients with cHC-CC, ICC, or HCC to detect YAP1 and SMAD2 and observed significant YAP1 activation (greater than grade 2, as defined in Table S1) in 70% of cHC-CCs and 60% of ICCs, but in only 23% of HCCs, 14% of nontumorous cholangiocytes (NT-Chol), and 6% of nontumorous hepatocytes (NT-Hep) (Fig. 6*A*). Furthermore, YAP1 activation showed a significant correlation with SMAD2 activation in these cHC-CCs and ICCs (Fig. 6*B*).

We next investigated whether chemical compounds or natural products able to inhibit YAP1 might have anticancer effects in the liver. To visualize Hippo pathway activity, we devised a sensitive system based on the H1299 human lung cancer cell line, in which endogenous YAP1 is highly activated. We engineered H1299 cells to express 10 copies of the *CTGF* TEAD-binding sequence plus the *luciferase* reporter gene (Fig. S6*A*) and screened 1,282 natural

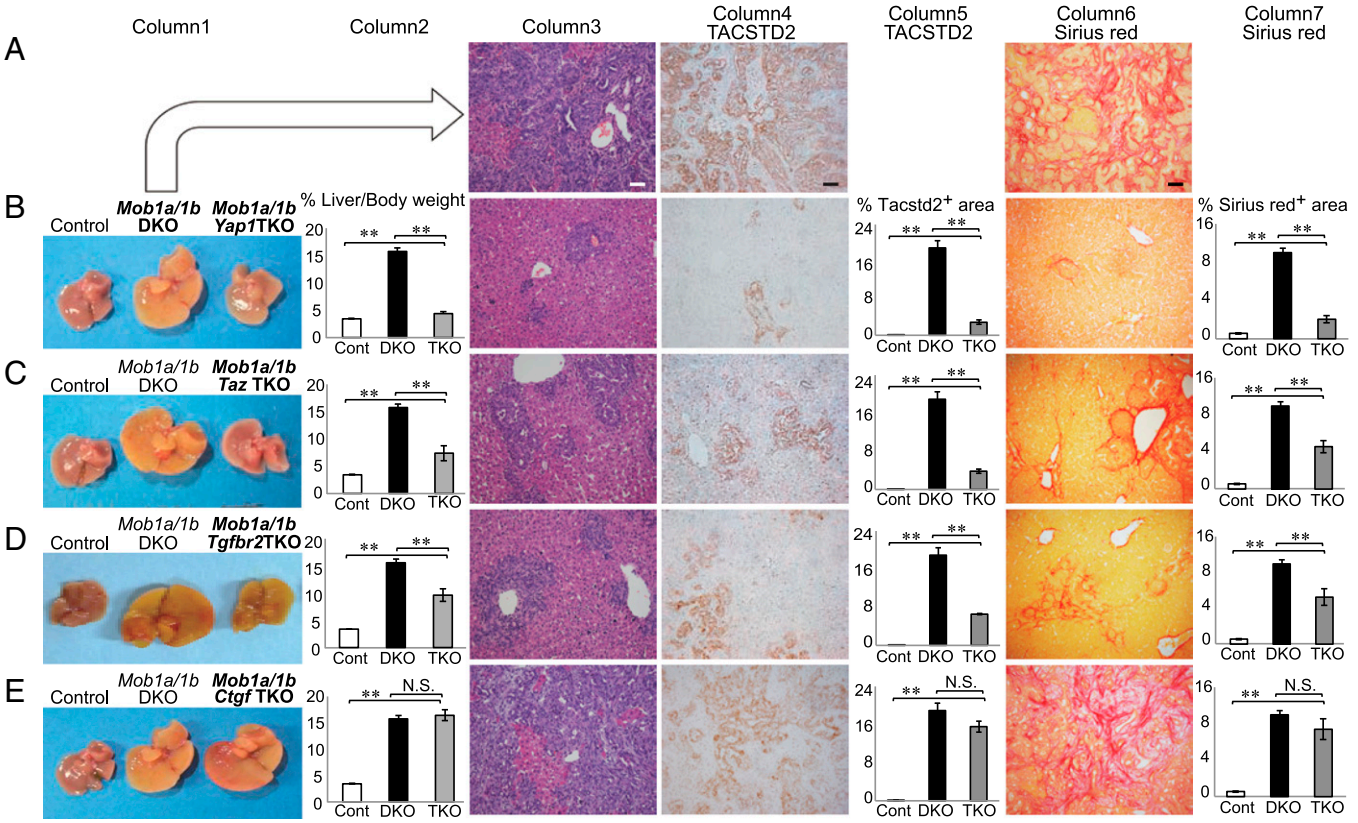

Fig. 5. *Mob1a/1b*-deficient liver phenotypes are dependent on *Yap1*, *Taz*, and *Tgfbs* but not on *Ctgf*. Analyses of livers from *Mob1a/1b* triple mutant (TKO) strains. Row *A*: Stained liver sections from *Mob1a/1b* DKO (*L*DKO) mice (*AlbCre;Mob1a*$^{flox/flox}$*;Mob1b*$^{-/-}$: $n = 27$) for comparison with TKO mouse liver sections below. Rows *B–E*: Comparative analyses of liver sections from control (*Mob1a*$^{flox/flox}$*;Mob1b*$^{-/-}$: $n = 25$), *Mob1a/1b*DKO ($n = 27$), and various *Mob1a/1b* TKO mutants at P14. (*B*) *Mob1a/1b* plus *Yap1* TKO (*AlbCre;Mob1a*$^{flox/flox}$*;Mob1b*$^{-/-}$*;Yap1*$^{flox/flox}$) ($n = 11$); (*C*) *Mob1a/1b* plus *Taz* TKO (*AlbCre;Mob1a*$^{flox/flox}$*;Mob1b*$^{-/-}$*;Taz*$^{-/-}$) ($n = 10$); (*D*) *Mob1a/1b* plus *Tgfbr2* TKO (*AlbCre; Mob1a*$^{flox/flox}$*;Mob1b*$^{-/-}$*;Tgfbr2*$^{flox/flox}$) ($n = 36$); and (*E*) *Mob1a/1b* plus *Ctgf* TKO (*AlbCre;Mob1a*$^{flox/flox}$*;Mob1b*$^{-/-}$*;Ctgf*$^{flox/flox}$) ($n = 14$). Column 1: Macroscopic views of livers of P14 mice of the indicated genotypes. Column 2: Liver weight as a percentage of body weight for the mice in Column 1. Column 3: H&E-stained liver sections. (Scale bar, 50 μm.) Column 4: TACSTD2 immunostaining. (Scale bar, 50 μm.) Column 5: Area of TACSTD2^{+} cells per field. Column 6: Sirius red staining to detect fibrosis. (Scale bar, 50 μm.) Column 7: Area of liver fibrosis per field. For columns 2, 5 and 7, data are the mean ± SEM $*P < 0.05$, $**P < 0.01$. N.S., not significant.

compounds and 10,240 synthetic compounds. Ivermectin (Fig. S6*B*) and its derivative milbemycin D (Fig. S6*C*) were identified as potential YAP1 inhibitors. Ivermectin is a well-tolerated antiparasitic macrocyclic lactone commonly used to treat river blindness (44), and both ivermectin and milbemycin D activate glutamate-gated chloride channels (45). Treatment of our modified H1299 cells in vitro with ivermectin or milbemycin D inhibited YAP1/TAZ activity and decreased *CTGF* expression in a dose-dependent manner (Fig. 7 *A–C* and Fig. S6 *D–F*). Dasatinib, a c-YES inhibitor that reduces YAP1 nuclear localization and activation, served as a positive control for these experiments. Ivermectin and milbemycin D also strongly suppressed the in vitro growth of both *im*Mob1DKOLP+Tmx cells and an NF2-deficient human mesothelioma cell line (NCI-H290) in which YAP1/TAZ is constitutively activated (Fig. 7 *D* and *E* and Fig. S6*G*). Cell growth inhibition by ivermectin was similar to that observed following application of siYAP1/TAZ (Fig. 7 *D* and *E*). Importantly, ivermectin treatment of *L*Mob1DKO mice for 5 d (P4–P8) reduced their hepatomegaly, accumulations of oval cells/immature cholangiocytes, excessive hepatic YAP1 activation (Fig. 7 *F* and *G*), and expression of YAP1/TAZ target proteins (Fig. 7*H*). Finally, we transfected the KKU-M213 line of human CC cells with Dox-dependent shYAP1/TAZ, xenografted these cells into *nude* mice, and allowed tumors to establish. Treatment of these mice for 18 d with cyclodextrin-conjugated ivermectin [ivermectin (−Dox); 10 mg/kg daily by i.p. injection] significantly inhibited tumor growth compared with control treated with DMSO (−Dox) (Fig. 7 *I* and *J*). This effect of ivermectin was comparable to that of shYAP1/TAZ treatment alone [DMSO (+Dox); Fig. 7*I*], and ivermectin did not further suppress the growth of shYAP1/TAZ-treated tumors [ivermectin (+Dox); Fig. 7*I*]. Finally, ivermectin significantly reduced the growth of tumors established by xenografting *im*Mob1DKOLP+Tmx cells into *nude* mice (Fig. S6*H*). These results suggest that antiparasitic macrocyclic lactones may aid in the treatment of liver cancers by blocking Hippo signaling.

Discussion

We have shown that loss of *Mob1a/1b* in mouse liver results in YAP1/TAZ activation and either early lethality associated with oval cell/immature cholangiocyte hyperplasia or later lethality associated with liver tumorigenesis. These data indicate that MOB1A/1B maintain oval cell quiescence and function as potent tumor suppressors in the liver. The liver phenotypes of *L*Mob1DKO mice are more dramatic than those of mice with liver-specific mutations of *Nf2* (14), *Sav1* (15, 16), or *Mst1/2* (17, 18), suggesting that MOB1A/1B are the most important elements of Hippo signaling in mammalian liver. We have also clarified that a major downstream effector of MOB1A/1B in the liver is the YAP1-TEAD1/4 pathway. This result is consistent with previous reports that YAP1-null mice show decreased cholangiocytes and increased hepatocyte apoptosis accompanied by steatosis (23), and that TEAD1/4 have stronger

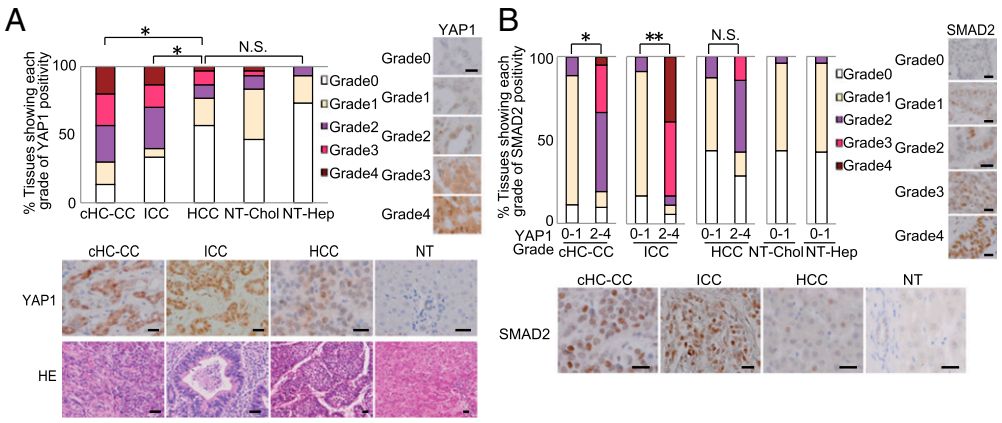

Fig. 6. Characterization of Hippo-YAP1 and TGF-β–SMADs pathways in human liver cancers. (*A*) (*Upper Left*) Percentages of cHC-CCs, ICCs, HCCs, nontumorous (NT) cholangiocytes (NT-Chol), and NT hepatocytes (NT-Hep) ($n = 30$) showing the indicated grades (Table S1) of YAP1 activation. (*Right*) Representative YAP1 grade 0–4 stainings. (*Lower Left*) Representative YAP1 and H&E stainings of a cHC-CC (grade 3 YAP1), ICC (grade 3), HCC (grade 2), and NT tissue (grade 0). (Scale bars, 50 μm.) (*B*) (*Upper Left*) Percentages of the tissues in *A* showing the indicated grades (Table S1) of SMAD2 activation. (*Right*) Representative SMAD2 grade 0–4 stainings. (*Lower Left*) Representative SMAD2 stainings of a cHC-CC (grade 3), ICC (grade 4), HCC (grade 2), and NT tissue (grade 1). (Scale bars, 50 μm.) $*P < 0.01$, $**P < 0.001$. N.S., not significant.

effects than TEAD2/3 on transcriptional targets in human liver cells (12). Finally, we have demonstrated that TAZ and TGF-β2/3 are also critical Hippo signaling effectors whose loss mitigates the liver phenotypes of *L*Mob1DKO mice.

We propose a model (Fig. S7*A*) in which loss of *Mob1a*/*1b* activates YAP1, resulting in impaired cell contact-dependent growth inhibition but increased hepatocyte dedifferentiation, oval cell proliferation, cell migration, EMT, and liver tumor formation. The increased oval cells/immature cholangiocytes and fibrosis in *L*Mob1DKO liver depend partially on increased TGF-β2/3 production by hepatocytes. Indeed, TGF-βs impair hepatocyte lineage differentiation, promote cholangiocyte lineage differentiation (42, 46), and increase EMT (30). Because SPP1 (osteopontin) produced by cholangiocytes also drives inflammatory cell infiltration, fibrosis, and cholangiocyte differentiation (47), some *Mob1a*/*1b*-deficient liver phenotypes may depend in part on SPP1 overexpression.

MOB1A/1B binding strongly augments LATS1/2 kinase activities (25). However, LATS1/2 had been considered unlikely to play a major role in mammalian liver because liver-specific loss of MST1/2 had no effect on LATS1/2 phosphorylation (18), and neither LATS1 KO nor liver-specific LATS2 KO mice show obvious liver phenotypes. More recently, it has been reported that *AlbCre;Lats1*$^{flox/flox}$*;Lats2*$^{flox/flox}$ mice display liver abnormalities that are strikingly similar to those of our *L*Mob1DKO mice (48), indicating that the MST–MOB1–LATS–YAP1 axis is important after all in mammalian liver.

In human cHC-CCs and ICCs, we observed frequent and strong YAP1 activation that correlated with increased SMAD2 activation. Nuclear translocation of YAP1/TAZ increases transcription of TGF-βs (11), and TGB-βs can activate and increase nuclear YAP1 via SMAD2/3 activation (Fig. S5 *C* and *D*). In addition, nuclear translocation of YAP1/TAZ enhances nuclear translocation of SMAD2/3 (33). These observations suggest that positive cross-talk exists between the TGF-β–SMAD and YAP1/TAZ pathways (Fig. S7*B*), providing signaling that may contribute to the phenotypes of both *L*Mob1DKO mice and patients with cHC-CC or ICC. Because TGF-β2/3 are transcriptional targets of YAP1/TAZ, abnormal elevation of YAP1/TAZ both increases production of TGF-β2/3 and stimulates SMAD-mediated transcription of TGF-β2/3 target genes. Coordinated targeting of YAP1/TAZ and TGF-β signaling may thus be an effective treatment for cHC-CCs and ICCs displaying dysregulated Hippo signaling.

Our library screen revealed that ivermectin (44) and milbemycin D inhibit YAP1 activity in vitro and in vivo. In parasites, these agents kill by activating glutamate-gated chloride channels and inducing membrane hyperpolarization. In mammalian cells, high concentrations of ivermectin not only activate chloride channels but also induce reactive oxygen species accumulation, block the β-catenin pathway, and inhibit the tumor-suppressive activity of PAK kinase (49–52). In addition, in virus-infected cells, ivermectin impairs the nuclear import of signaling molecules mediated by α/β importins (53). This inhibition of nuclear import may not only prevent nuclear localization and activation of YAP1 but perhaps also that of other targets that could contribute to hepatocarcinogenesis. Although the precise mechanism(s) underlying ivermectin's inhibition of YAP1 is not yet clear, this agent does not seem to strongly activate MST, MOB, or LATS (Fig. S8), indicating that the effect may not be due to interference with canonical Hippo signaling. Nevertheless, it is relevant that, even at high doses, ivermectin has very few adverse effects on humans (49). This benign profile could potentially accelerate the testing of this agent for cHC-CC or ICC treatment in patients.

In conclusion, our results demonstrate that (*i*) MOB1A/1B constitute the most important hub of Hippo signaling in mammalian liver, restricting liver cell growth and maintaining hepatocyte stem/progenitor cell quiescence; (*ii*) the phenotypes of *L*Mob1DKO mice are largely dependent on YAP1 and partly dependent on TAZ and TGF-β2/3; (*iii*) loss of MOB1A/1B (activation of YAP1) is an important driver of liver tumorigenesis, especially cHC-CCs and ICCs, in both mice and humans; and (*iv*) antiparasitic macrocyclic lactones inhibit YAP1 activation in vitro and in vivo. Our data point to a new therapeutic approach for cHC-CC and ICC patients based on inhibition of MOB1-YAP1/TAZ and/or TGF-βs–SMADs signaling.

Materials and Methods

Mice. Base mouse strains used in this study were as follows: *AlbCre-Tg* (Jackson), *Mob1a*$^{flox/flox}$*;Mob1b*$^{-/-}$ (28), *Rosa26-LSL-YFP* reporter (36), *AlbCreER-Tg* (54), *Rosa26CreER-Tg* (55), *Yap1*$^{flox/flox}$ (Knockout Mouse Project Repository), *Taz*$^{-/-}$ (56), *Tgfbr2*$^{flox/flox}$ (57), and *Ctgf*$^{flox/flox}$ (58).

Generation of *L*Mob1DKO Mice and Related Strains. Liver-specific *Mob1a/1b* double-homozygous mutant mice (*AlbCre;Mob1a*$^{flox/flox}$*;Mob1b*$^{-/-}$ mice; designated *L*Mob1DKO) were generated by mating *AlbCre*-Tg mice to *Mob1a*$^{flox/flox}$*;Mob1b*$^{-/-}$ mice. *Mob1a*$^{flox/flox}$*;Mob1b*$^{-/-}$, *AlbCre;Mob1a*$^{+/+}$*;Mob1b*$^{-/-}$, *AlbCre;Mob1a*$^{flox/flox}$*;Mob1b*$^{+/+}$ and *AlbCre;Mob1a*$^{+/+}$*;Mob1b*$^{+/+}$ mice were indistinguishable in pilot experiments examining body weight, histology, and lifespan (discussed below). *AlbCre*-Tg mice were of the C57BL/6 background, and *Mob1a*$^{flox/flox}$*;Mob1b*$^{-/-}$ mice were back-crossed to C57BL/6 for

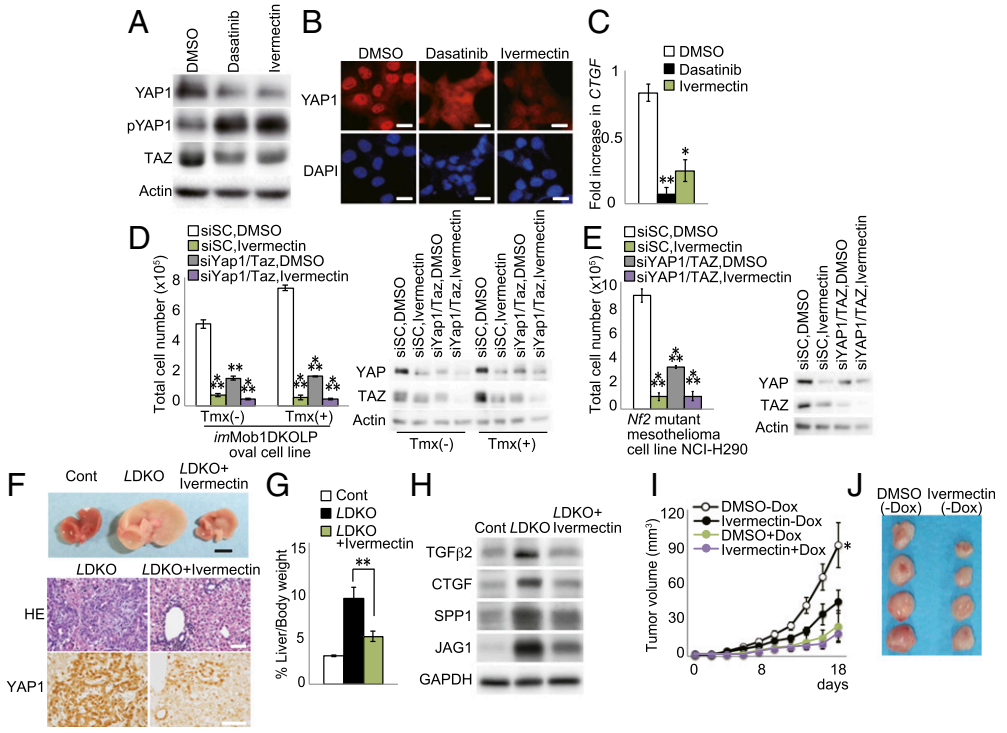

Fig. 7. Ivermectin blocks YAP1 activity in vitro and in vivo. (*A* and *B*) H1299 cells were treated with vehicle (DMSO), dasatinib, or ivermectin for 24 h. (*A*) Immunoblot detecting YAP1, pYAP1, and TAZ protein. (*B*) Immunostaining detecting YAP1 (red). (Scale bars, 20 μm.) (*C*) Quantitative RT-PCR of *Ctgf* mRNA in cells in *B* and *C*. Data are the mean ± SEM ($n = 3$). (*D* and *E*) (*Left*) Total numbers of *im*Mob1DKOLP ± Tmx (*D*) and NCI-H290 (*E*) cells that were transfected with siScramble (siSC) or siYAP1/TAZ, and treated with DMSO or ivermectin for 3 d. Tmx was administered 5 d before cell plating. Data are the mean ± SEM ($n = 3$). (*Right*) Immunoblots detecting inhibition of YAP1/TAZ by siRNA or ivermectin. (*F*) Representative macroscopic analyses (*Top*) (Scale bar, 5 mm) and H&E staining and YAP1 immunostaining (*Bottom*) (Scale bars, 50 μm) of livers from DMSO-treated control mice and *L*DKO mice treated with DMSO or ivermectin for 5 d (P4–P8) ($n = 7$). (*G*) Liver weight as a percentage of body weight for the mice in *F* at P10. Data are the mean ± SEM ($n = 7$). (*H*) Immunoblot detecting the indicated YAP1 downstream transcriptional target proteins in the livers of the mice in *F*. GAPDH, loading control. (*I* and *J*) Human CC cells (KKU-M213) were transfected with Dox-dependent shYAP1/TAZ and xenografted s.c. into *nude* mice. After visual detection of tumors, mice were treated with DMSO or ivermectin for 18 d and supplied with normal drinking water or water containing Dox. (*I*) Tumor growth in control (DMSO-Dox; $n = 38$), ivermectin-treated (ivermectin-DOX; $n = 50$), YAP1/TAZ-inactivated (DMSO+Dox; $n = 12$), and ivermectin plus YAP1/TAZ-inactivated (ivermectin+DOX; $n = 12$) mice. Data are the mean ± SEM. (*J*) Macroscopic view of xenografted tumors in mice in *I* at 18 d posttreatment with ivermectin plus normal drinking water. $^*P < 0.05$, $^{**}P < 0.01$, $^{***}P < 0.001$.

more than six generations. *Mob1a*$^{flox/flox}$*;Mob1b*$^{-/-}$ mice without the *AlbCre-Tg* allele were usually chosen to serve as controls. The deletion frequency of the *Mob1a*^{flox} allele was confirmed by genomic Southern blotting using the probe indicated in Fig. S1*A*. Primers used for genotyping PCR are listed in Table S2. The frequency of *Mob1A* deletion in hepatocytes and cholangiocytes (Fig. S1*C*) was determined by PCR analysis of cells microdissected using a Leica LMD6000 instrument.

To visualize cells with *Mob1a/1b* deletion, *L*Mob1DKO mice were crossed to *Rosa26-LSL-YFP* reporter mice. To induce Cre-mediated deletion of *Mob1a/1b* in liver cells of adult mice, we generated *AlbCreER;Mob1a*$^{flox/flox}$*;Mob1b*$^{-/-}$ and *Rosa26CreER;Mob1a*$^{flox/flox}$*;Mob1b*$^{-/-}$ mice using *AlbCreER-Tg* mice or *Rosa26CreER-Tg* mice, respectively, and treated them with tamoxifen as described below.

AlbCre;Mob1a$^{flox/flox}$*;Mob1b*$^{-/-}$*;Yap1*$^{flox/flox}$, *AlbCre;Mob1a*$^{flox/flox}$*;Mob1b*$^{-/-}$*;Taz*$^{-/-}$, *AlbCre;Mob1a*$^{flox/flox}$*;Mob1b*$^{-/-}$*;Tgfbr2*$^{flox/flox}$, *and AlbCre;Mob1a*$^{flox/flox}$*;Mob1b*$^{-/-}$*;Ctgf*$^{flox/flox}$, TKO mice were generated by mating *AlbCreMob1a*$^{flox/flox}$*;Mob1b*$^{-/-}$ mice with *Yap1*$^{flox/flox}$, *Taz*$^{-/-}$, *Tgfbr2*$^{flox/flox}$, or *Ctgf*$^{flox/flox}$ mutant mice, respectively. All protocols for animal experiments were approved by the Animal Research Committee of Kyushu University. All animal experiments adhered to the criteria outlined in ref. 59.

Southern Blotting. Genomic Southern blots were performed as described (60). Agarose gels were transferred to nylon membranes (GE Healthcare) and hybridized to the probe described in Fig. S1*A*.

Isolation of Mouse Liver Cells. Hepatocytes were isolated from mice on various days after birth using an in situ two-step collagenase liver perfusion method as previously described (61). Residual liver cells containing Glisson's sheath were further exposed to 0.05% collagenase/ 0.1% Pronase for 30 min to generate a single-cell suspension. This suspension was mixed with the isolated hepatocytes to create a preparation deemed to be "total liver cells," which was used for analysis of total cell numbers and for primary cultures.

Liver Histology. Liver tissues were fixed in phosphate-buffered 4% (wt/vol) paraformaldehyde (PFA) and embedded in paraffin, and sections (5 μm) were mounted on slides for H&E staining or immunohistochemical (IHC) analysis. IHC analysis was performed using the antibodies (Abs) and protocol described below. Liver tissues were also stained using Elastica Masson and Sirius Red according to standard protocols.

Immunostaining. Tissues were fixed in 4% (wt/vol) PFA or neutral-buffered 10% (vol/vol) formalin and embedded in paraffin, or fixed in 1% (wt/vol) PFA and snap-frozen in optimal cutting temperature compound and sectioned (5 μm). Fixed sections or cells fixed in 4% (wt/vol) PFA were incubated overnight at 4 °C with primary Abs. Primary Abs used for IHC and immunocytochemistry recognized: HNF4A (sc-8987; Santa Cruz), KRT19 (TROMA-III-c; Hybrydomabank), KRT7 (MAB3226; Millipore), ALB (A90-134A; Bethyl), CDH1 (E-Cadherin; 610181; BD Transduction Laboratories), TACSTD2 (TROP2; BAF1122; R&D), A6 (62), DLK1 (AM26511AF-N; Acris), AFP(688031; MP Biomedicals), KIT (55353; BD), THY1 (11-0902-85; eBio), CD45 (12-0451-83; eBio), CD31 (553371; BD), VIM (Vimentin; V2258; Sigma), ACTA2 (αSMA; ab5694; Abcam), YFP/GFP (ab6673; Abcam), YAP1 (WH0010413M1; Sigma), SMAD2 (sc-101153; Santa Cruz), SMAD2/3 (sc-8332; Santa Cruz), TGF-β2 (ab36495; Abcam), TGF-β3 (BS1363; Bioworld Technology), CTGF (sc-14939; Santa Cruz), JAG1 (Jagged1; sc-8303; Santa Cruz), or SPP1 (AF808; R&D). Secondary Abs were tagged with Alexa Fluor488 or Alexa Fluor568 (Molecular Probes). Anti-rabbit/mouse-HRP was used for DAB staining. Nuclei were visualized using DAPI (Dojindo) or Giemsa staining.

Tumor Analyses. Spontaneous tumor formation was monitored in 69 *AlbCre;Mob1a*$^{flox/flox}$*;Mob1b*$^{-/-}$ and 26 *Mob1a*$^{flox/flox}$*;Mob1b*$^{-/-}$ mice over a 60-wk

observation period. Mice were killed when they became morbid (humane endpoint). The onset of liver tumors was confirmed by macroscopic analysis, and sections of tumors were prepared for H&E staining.

Generation of Adult Liver-Specific *Mob1a/1b*-Deficient Mice. To induce Cre-mediated deletion of *Mob1a/1b* in liver cells of adult mice, *AlbCreER;Mob1a*$^{flox/flox}$*;Mob1b*$^{-/-}$ mice (5 wk of age) received i.p. injection of 0.5 mg Tmx (5 mg/mL; i.p. 0.1 mL/d for 7 d). Mice were monitored daily for the onset of tumors.

BrdU Incorporation. Mice at P10 were i.p. injected with BrdU (50 μg/g body weight; Roche). Mice were killed 1 h later and livers were harvested and fixed in 100% methanol for 12 h. Fixed livers were embedded in paraffin and cut into 5-μm sections. BrdU incorporation was visualized by immunostaining with anti-BrdU Ab (5292; Cell Signaling). Hepatocytes and cholangiocytes were identified by immunostaining with anti-HNF4A (sc-8987; Santa Cruz) and anti-KRT19 (TROMA-III-c; Hybrydomabank) Abs, respectively. BrdU incorporation was assessed in at least 1,000 HNF4A$^+$ hepatocytes and 200 KRT19$^+$ cholangiocytes per mouse.

TUNEL Assay. Apoptosis of liver cells was determined by TUNEL assay using the In Situ Cell Death Detection Kit (Roche) according to the manufacturer's instructions. Nuclei were visualized using DAPI.

Establishment of the *im*Mob1DKOLP Cell Line and Induction of Differentiation. To generate a Tmx-inducible murine *Mob1a/1b*-deficient liver progenitor cell line, liver cells were isolated from 5-wk-old *Rosa26CreER;Mob1*$^{flox/flox}$*;Mob1b*$^{-/-}$ mice (without Tmx) using the collagenase perfusion technique described above. Liver cells were cultured (3×10^5 per 6-cm dish) in Williams' Medium E (Sigma) supplemented with 10% (vol/vol) FCS. The medium was changed twice per week and the culture was maintained for 3 mo until a single spontaneously transformed colony appeared. This colony was isolated, recloned using limiting dilution, and expanded to generate the *im*Mob1DKOLP cell line. Inducible loss of *Mob1a/1b* in these cells was confirmed by treating them with Tmx (1μM) for at least 5 d, followed by analyses of mRNA expression by RT-PCR and protein expression by immunoblotting.

To induce hepatocyte differentiation, *im*Mob1DKOLP cells (500 cells per 20 μL) were cultured for 2 d using the hanging drop method, followed by culture for an additional 9 d in multiwell plates that were coated with Matrigel (BD Bioscience) and filled with serum-free Williams' Medium E containing 1 μM dexamethasone and 10 ng/mL OncostatinM (R&D). To induce cholangiocyte differentiation, *im*Mob1DKOLP cells (500 cells per 20 μL) were precultured in hanging drops and then cultured for 14 d in 3D cultures (63) containing 0.24 mg/mL type I collagen (Cellmatrix type I-A; Nitta Gelatin), 10% (vol/vol) FCS, and 10 ng/mL TNFα (R&D).

Proliferation of *im*Mob1DKOLP Cells. For cell growth analysis, *im*Mob1DKOLP cells (2.5×10^4 per well in 24-well plates) were cultured for up to 9 d in Williams' E medium supplemented with 10% (vol/vol) FCS, with or without Tmx (1 μM).

Quantitative RT-PCR. Total RNA was extracted from *im*Mob1DKOLP cells cultured with or without Tmx (1 μM) for 6 or 10 d, or from whole livers of *AlbCre;Mob1*$^{flox/flox}$*;Mob1b*$^{-/-}$ (*L*Mob1DKO) and control mice at P14, using RNAiso (Takara) according to the manufacturer's protocol. Total RNA (1 μg) was reverse-transcribed using the Transcriptor First Strand cDNA Synthesis Kit (Roche) after DNase (Toyobo) treatment. Sequences of specific primer sets used for RT-PCR are listed in Table S3. The mRNA level of a specific gene in the mutant was expressed as the fold increase over the corresponding control value.

Immunoblotting. Immunoblotting was carried out using a standard protocol and primary Abs recognizing: pMST1/2 (3681; Cell Signaling), MST1 (3682; Cell Signaling), MOB1A/1B (13730; Cell Signaling), pYAP1 (4911; Cell Signaling), YAP1 (4912; Cell Signaling), pTAZ (sc-17610; Santa Cruz), TAZ (4883; Cell Signaling), pLATS1 (9159; Cell Signaling), LATS1 (3477; Cell Signaling), CTGF (sc-14939; Santa Cruz), SPP1 (AF808; R&D), JAG1 (sc-8303; Santa Cruz), TGF-β2 (ab36495; Abcam), TGF-β3 (BS1363; Bioworld Technology), CCL2 (NBP2-22115S; Novus), NOTCH1 IC (ab8952; Abcam), NOTCH2 IC (ab8926; Abcam), HES1 (ab71559; Abcam), pSMAD2 (AB3849; Millipore), SMAD2/3 (sc-8332; Santa Cruz), ACTIN (A2066; Sigma), or GAPDH (sc-25778; Santa Cruz). Primary Abs were detected using HRP-conjugated secondary Abs (Cell Signaling).

Cell Migration. Migration of *im*Mob1DKOLP cells was assayed using Transwell chambers (5-μm pore size; Costar). *im*Mob1DKOLP cells precultured with or without Tmx (1μM) for 6 d were seeded in the upper Transwell chamber in 0.5% BSA/Williams' Medium E (1×10^4 cells per well), and 10% (vol/vol) FCS/Williams' Medium E was added to the bottom chamber. After 24 h, cells remaining in the upper chamber were removed and cells in the bottom chamber were fixed with 4% (wt/vol) PFA, stained with crystal violet, and counted under a light microscope. Four fields per chamber were evaluated.

siRNA Transfection. siRNA targeting of *Yap1*, *Taz*, *Tead1*, *Tead2*, *Tead3*, *Tead4*, *Smad2*, or *Smad3* expression was performed using the specific siRNA oligonucleotides listed in Table S4. Transfection of siRNA oligonucleotides (10 nM) into exponentially-growing *im*Mob1DKOLP cells or *NF2*-deleted NCI-H290 human mesothelioma cells (64) (3×10^4 per well in 24-well plates) was performed using Lipofectamine RNAiMAX (Invitrogen) following the manufacturer's protocol. At 72 h posttransfection, total cell numbers were evaluated and total RNA was subjected to RT-PCR to detect inhibition of mRNA expression.

Clinical Samples. Surgically obtained human cHC-CCs ($n = 30$), ICCs ($n = 30$), and HCCs ($n = 30$) were acquired from the Department of Surgery of Kyushu University Beppu Hospital and affiliated hospitals. Resected cancer tissues were fixed in formalin and stained with anti-YAP1 Ab (WH0010413M1; Sigma) or anti-SMAD2 Ab (sc-101153; Santa Cruz) using a standard protocol. Resected nontumorous healthy cholangiocytes ($n = 30$) and hepatocytes ($n = 30$) were examined as controls. Grades of YAP1 and SMAD2 activation were defined as described in Table S1. The clinical sample study design was approved by the Kyushu University Institutional Review Board for Clinical Research and informed consent was obtained from each patient.

Chemical Screening. H1299 cells were engineered to express a reporter construct containing 10 copies of the TEAD-binding sequence from the *CTGF* gene plus the firefly *luciferase* gene (Fig. S6*A*). Reporter cells were seeded in 384-well microplates (1,000 cells per well) and cultured overnight in a CO_2 incubator. A library of natural compounds (1,282 samples) and a library of synthetic compounds (10,240 samples) were screened for the ability to inhibit Hippo signaling by dispensing each natural compound (final concentration 10 μg/mL) or synthetic compound (final concentration 25 μM) into cell cultures. After 24-h treatment with screening compounds, reporter luciferase activity and cell viability were measured using the Picagene BrilliantStar-LT Luminescence Kit (307–15373; Toyo B-Net) and Cell Counting Kit-8 (CK04; Dojindo), respectively, according to the manufacturers' instructions. Compounds that markedly suppressed reporter activity but exerted low cell toxicity were considered to be positive hits. Positive hits included the antiparasitic macrocyclic lactones ivermectin and milbemycin D.

In Vitro Effects of Macrocyclic Lactones. To determine the effects of positive hit agents on YAP1 activation in vitro, H1299 cells (3×10^5 per well in six-well plates) were cultured for 24 h in RPMI1640 medium containing ivermectin (10 μM; Sigma), milbemycin D (10 μM; BioAustralis Fine Chemicals), vehicle (DMSO, negative control), or Dasatinib (positive control; Abcam). Expression of YAP1 protein and mRNA encoding the YAP1 downstream target *CTGF* were analyzed by immunoblotting, immunocytochemistry, and RT-PCR. To determine the effects of agents on cell growth, *im*Mob1DKOLP ± Tmx cells or NCI-H290 cells (3×10^4 per well in 24-well plates) treated with siYAP1/TAZ or siScramble were cultured for 3 d in RPMI1640 medium containing ivermectin (10 μM) or milbemycin D (10 μM).

In Vivo Effects of Ivermectin. To determine the in vivo effects of ivermectin on the liver phenotypes of *L*Mob1DKO mice, we treated control and *L*Mob1DKO mice (P4; $n = 7$ per group) with ivermectin (2 mg/kg, i.p.) daily for 5 d. Liver weight and histology were analyzed at P10.

Tumor Growth in Xenografted *nude* Mice. Human cholangiocellular cancer cells (KKU-M213; 1×10^5) that had been transfected with Dox-dependent shYAP1/TAZ, or MOB1-deficient murine liver progenitor cells (*im*Mob1DKOLP cells; 2×10^5), were injected s.c. into the flanks of 8- to 10-wk-old female BALB/cAJcl-*nu/nu* mice (CLEA Japan). After visual detection of tumors (usually by 8 d postinjection), mice were treated with 45% (wt/vol) cyclodextrin-conjugated ivermectin (10 mg/kg, i.p., daily) or cyclodextrin carrier alone and supplied with normal drinking water or water containing Dox (2 mg/mL). Tumor volumes were measured every 2 d using calipers.

Statistics. Where appropriate, results are expressed as the mean ± SEM of the indicated number of mice or cultures per group. Statistical differences were determined using the Student's *t* test or Welch's *t* test. Survival curves were calculated using the Kaplan–Meier method and analyzed with the log-rank test. For clinical samples, statistical differences between groups were determined using the χ^2 test and the JMP software package (SAS Institute).

ACKNOWLEDGMENTS. We thank A. Miyajima and K. Miyazono (both of Tokyo University); K. Enomoto (Akita University); M. Fukumoto (Tohoku University); M. Kasagi, A. Fujimoto, A. Suzuki, and M. Suzuki (all of Kyushu University); and S. Maegawa, J. Utsumi, F. Ishikawa, M. Seiki, and T. Noda (all of P-DIRECT) for expert technical assistance and helpful discussions. We thank J. Roes (University College London) and P. Chambon (Université de Strasbourg) for *Tgfbr2flox* and *AlbCreER* Tg mice, respectively. We thank V. M. Factor (National Institutes of Health) for A6 antibody. This work was supported by grants from the Ministry of Education, Culture, Sports and Technology of Japan (to A.S., M.N., and J.W.); P-DIRECT (to A.S.); the Cooperative Research Project Program of the Medical Institute of Bioregulation, Kyushu University; the Uehara Memorial Foundation (to A.S.); the Takeda Medical Foundation (to A.S.); and the Mitsui Life Social Welfare Foundation (to K.S.).

1. Llovet JM, Burroughs A, Bruix J (2003) Hepatocellular carcinoma. *Lancet* 362(9399): 1907–1917.
2. Parkin DM, Bray F, Ferlay J, Pisani P (2001) Estimating the world cancer burden: Globocan 2000. *Int J Cancer* 94(2):153–156.
3. Anonymous (1992) Prevention and control of neurofibromatosis: Memorandum from a joint WHO/NNFF meeting. *Bull World Health Organ* 70(2):173–182.
4. Edgar BA (2006) From cell structure to transcription: Hippo forges a new path. *Cell* 124(2):267–273.
5. Hergovich A (2011) MOB control: Reviewing a conserved family of kinase regulators. *Cell Signal* 23(9):1433–1440.
6. Nishio M, Otsubo K, Maehama T, Mimori K, Suzuki A (2013) Capturing the mammalian Hippo: Elucidating its role in cancer. *Cancer Sci* 104(10):1271–1277.
7. Dupont S, et al. (2011) Role of YAP/TAZ in mechanotransduction. *Nature* 474(7350): 179–183.
8. Kanai F, et al. (2000) TAZ: A novel transcriptional co-activator regulated by interactions with 14-3-3 and PDZ domain proteins. *EMBO J* 19(24):6778–6791.
9. Zhao B, et al. (2008) TEAD mediates YAP-dependent gene induction and growth control. *Genes Dev* 22(14):1962–1971.
10. Anakk S, et al. (2013) Bile acids activate YAP to promote liver carcinogenesis. *Cell Reports* 5(4):1060–1069.
11. Yi C, et al. (2013) The p130 isoform of angiomotin is required for Yap-mediated hepatic epithelial cell proliferation and tumorigenesis. *Sci Signal* 6(291):ra77.
12. Tschaharganeh DF, et al. (2013) Yes-associated protein up-regulates Jagged-1 and activates the Notch pathway in human hepatocellular carcinoma. *Gastroenterology* 144(7):1530–1542.e1512.
13. Zhao B, Li L, Tumaneng K, Wang CY, Guan KL (2010) A coordinated phosphorylation by Lats and CK1 regulates YAP stability through SCF(beta-TRCP). *Genes Dev* 24(1):72–85.
14. Benhamouche S, et al. (2010) Nf2/Merlin controls progenitor homeostasis and tumorigenesis in the liver. *Genes Dev* 24(16):1718–1730.
15. Lu L, et al. (2010) Hippo signaling is a potent in vivo growth and tumor suppressor pathway in the mammalian liver. *Proc Natl Acad Sci USA* 107(4):1437–1442.
16. Lee JH, et al. (2008) A crucial role of WW45 in developing epithelial tissues in the mouse. *EMBO J* 27(8):1231–1242.
17. Zhou D, et al. (2009) Mst1 and Mst2 maintain hepatocyte quiescence and suppress hepatocellular carcinoma development through inactivation of the Yap1 oncogene. *Cancer Cell* 16(5):425–438.
18. Song H, et al. (2010) Mammalian Mst1 and Mst2 kinases play essential roles in organ size control and tumor suppression. *Proc Natl Acad Sci USA* 107(4):1431–1436.
19. Zender L, et al. (2006) Identification and validation of oncogenes in liver cancer using an integrative oncogenomic approach. *Cell* 125(7):1253–1267.
20. Camargo FD, et al. (2007) YAP1 increases organ size and expands undifferentiated progenitor cells. *Curr Biol* 17(23):2054–2060.
21. Dong J, et al. (2007) Elucidation of a universal size-control mechanism in Drosophila and mammals. *Cell* 130(6):1120–1133.
22. Yimlamai D, et al. (2014) Hippo pathway activity influences liver cell fate. *Cell* 157(6): 1324–1338.
23. Zhang N, et al. (2010) The Merlin/NF2 tumor suppressor functions through the YAP oncoprotein to regulate tissue homeostasis in mammals. *Dev Cell* 19(1):27–38.
24. Schlegelmilch K, et al. (2011) Yap1 acts downstream of α-catenin to control epidermal proliferation. *Cell* 144(5):782–795.
25. Stavridi ES, et al. (2003) Crystal structure of a human Mob1 protein: toward understanding Mob-regulated cell cycle pathways. *Structure* 11(9):1163–1170.
26. Lignitto L, et al. (2013) Proteolysis of MOB1 by the ubiquitin ligase praja2 attenuates Hippo signalling and supports glioblastoma growth. *Nat Commun* 4:1822.
27. Kosaka Y, et al. (2007) Clinical significance of the loss of MATS1 mRNA expression in colorectal cancer. *Int J Oncol* 31(2):333–338.
28. Nishio M, et al. (2012) Cancer susceptibility and embryonic lethality in Mob1a/1b double-mutant mice. *J Clin Invest* 122(12):4505–4518.
29. Xu MZ, et al. (2009) Yes-associated protein is an independent prognostic marker in hepatocellular carcinoma. *Cancer* 115(19):4576–4585.
30. Ikushima H, Miyazono K (2010) TGFbeta signalling: A complex web in cancer progression. *Nat Rev Cancer* 10(6):415–424.
31. Bierie B, Moses HL (2006) Tumour microenvironment: TGFbeta: The molecular Jekyll and Hyde of cancer. *Nat Rev Cancer* 6(7):506–520.
32. Kitisin K, et al. (2007) Tgf-Beta signaling in development. *Sci STKE* 2007(399):cm1.
33. Varelas X, et al. (2008) TAZ controls Smad nucleocytoplasmic shuttling and regulates human embryonic stem-cell self-renewal. *Nat Cell Biol* 10(7):837–848.
34. Varelas X, et al. (2010) The Crumbs complex couples cell density sensing to Hippo-dependent control of the TGF-β-SMAD pathway. *Dev Cell* 19(6):831–844.
35. Postic C, Magnuson MA (2000) DNA excision in liver by an albumin-Cre transgene occurs progressively with age. *Genesis* 26(2):149–150.
36. Srinivas S, et al. (2001) Cre reporter strains produced by targeted insertion of EYFP and ECFP into the ROSA26 locus. *BMC Dev Biol* 1:4.
37. Germain L, Blouin MJ, Marceau N (1988) Biliary epithelial and hepatocytic cell lineage relationships in embryonic rat liver as determined by the differential expression of cytokeratins, alpha-fetoprotein, albumin, and cell surface-exposed components. *Cancer Res* 48(17):4909–4918.
38. Bird TG, Lorenzini S, Forbes SJ (2008) Activation of stem cells in hepatic diseases. *Cell Tissue Res* 331(1):283–300.
39. Kuwahara R, et al. (2008) The hepatic stem cell niche: Identification by label-retaining cell assay. *Hepatology* 47(6):1994–2002.
40. Hirabayashi S, et al. (2008) Threonine 74 of MOB1 is a putative key phosphorylation site by MST2 to form the scaffold to activate nuclear Dbf2-related kinase 1. *Oncogene* 27(31):4281–4292.
41. Sekiya S, Suzuki A (2014) Hepatocytes, rather than cholangiocytes, can be the major source of primitive ductules in the chronically injured mouse liver. *Am J Pathol* 184(5): 1468–1478.
42. Takayama K, et al. (2014) CCAAT/enhancer binding protein-mediated regulation of TGFβ receptor 2 expression determines the hepatoblast fate decision. *Development* 141(1):91–100.
43. Ma Y, Yang Y, Wang F, Wei Q, Qin H (2015) Hippo-YAP signaling pathway: A new paradigm for cancer therapy. *Int J Cancer* 137(10):2275–2286.
44. Traore MO, et al. (2012) Proof-of-principle of onchocerciasis elimination with ivermectin treatment in endemic foci in Africa: Final results of a study in Mali and Senegal. *Plos Neglect Trop D* 6(9):e1825.
45. Wang CC, Pong SS (1982) Actions of avermectin B1a on GABA nerves. *Prog Clin Biol Res* 97:373–395.
46. Akkari L, et al. (2010) Cell shape and TGF-beta signaling define the choice of lineage during in vitro differentiation of mouse primary hepatic precursors. *J Cell Physiol* 225(1):186–195.
47. Wang X, et al. (2014) Osteopontin induces ductular reaction contributing to liver fibrosis. *Gut* 63(11):1805–1818.
48. Chen Q, et al. (2015) Homeostatic control of Hippo signaling activity revealed by an endogenous activating mutation in YAP. *Genes Dev* 29(12):1285–1297.
49. Dadarkar SS, Deore MD, Gatne MM (2007) Comparative evaluation of acute toxicity of ivermectin by two methods after single subcutaneous administration in rats. *Regul Toxicol Pharmacol* 47(3):257–260.
50. Sharmeen S, et al. (2010) The antiparasitic agent ivermectin induces chloride-dependent membrane hyperpolarization and cell death in leukemia cells. *Blood* 116(18): 3593–3603.
51. Melotti A, et al. (2014) The river blindness drug Ivermectin and related macrocyclic lactones inhibit WNT-TCF pathway responses in human cancer. *EMBO Mol Med* 6(10): 1263–1278.
52. Hashimoto H, Messerli SM, Sudo T, Maruta H (2009) Ivermectin inactivates the kinase PAK1 and blocks the PAK1-dependent growth of human ovarian cancer and NF2 tumor cell lines. *Drug Discov Ther* 3(6):243–246.
53. Wagstaff KM, Sivakumaran H, Heaton SM, Harrich D, Jans DA (2012) Ivermectin is a specific inhibitor of importin α/β-mediated nuclear import able to inhibit replication of HIV-1 and dengue virus. *Biochem J* 443(3):851–856.
54. Schuler M, Dierich A, Chambon P, Metzger D (2004) Efficient temporally controlled targeted somatic mutagenesis in hepatocytes of the mouse. *Genesis* 39(3):167–172.
55. Badea TC, Wang Y, Nathans J (2003) A noninvasive genetic/pharmacologic strategy for visualizing cell morphology and clonal relationships in the mouse. *J Neurosci* 23(6): 2314–2322.
56. Makita R, et al. (2008) Multiple renal cysts, urinary concentration defects, and pulmonary emphysematous changes in mice lacking TAZ. *Am J Physiol Renal Physiol* 294(3):F542–F553.
57. Cazac BB, Roes J (2000) TGF-beta receptor controls B cell responsiveness and induction of IgA in vivo. *Immunity* 13(4):443–451.
58. Liu S, Shi-wen X, Abraham DJ, Leask A (2011) CCN2 is required for bleomycin-induced skin fibrosis in mice. *Arthritis Rheum* 63(1):239–246.
59. National Academy of Sciences (2011) *Guide for the Care and Use of Laboratory Animals* (National Academies, Washington, DC), 8th Ed.
60. Suzuki A, et al. (1997) Brca2 is required for embryonic cellular proliferation in the mouse. *Genes Dev* 11(10):1242–1252.
61. Nishikawa Y, et al. (2005) Transdifferentiation of mature rat hepatocytes into bile duct-like cells in vitro. *Am J Pathol* 166(4):1077–1088.
62. Engelhardt NV, et al. (1990) Common antigens of mouse oval and biliary epithelial cells. Expression on newly formed hepatocytes. *Differentiation* 45(1):29–37.
63. Sone M, et al. (2012) Recovery of mature hepatocytic phenotype following bile ductular transdifferentiation of rat hepatocytes in vitro. *Am J Pathol* 181(6):2094–2104.
64. Murakami H, et al. (2011) LATS2 is a tumor suppressor gene of malignant mesothelioma. *Cancer Res* 71(3):873–883.